

Published in final edited form as:

Cancer Res. 2011 April 15; 71(8): 2826–2837. doi:10.1158/0008-5472.CAN-10-2834.

Mathematical modelling predicts synergistic anti-tumor effects of combining a macrophage-based, hypoxia-targeted, gene therapy with chemotherapy

Markus R Owen¹, I Johanna Stamper^{1,2}, Munitta Muthana³, Giles W Richardson⁴, Jon Dobson^{5,6}, Claire E Lewis³, and Helen M Byrne¹

¹ Centre for Mathematical Medicine and Biology, School of Mathematical Sciences, University of Nottingham, Nottingham NG7 2RD, UK.

² Department of Physics, University of Alabama at Birmingham, Birmingham, AL 35294-1170, USA.

³ Department of Infection & Immunity, University of Sheffield Medical School, Sheffield, S10 2RX, UK.

⁴ School of Mathematics, University of Southampton, Southampton, SO17 1BJ, UK.

⁵ Institute for Science and Technology in Medicine, Keele University School of Medicine, Stoke-on-Trent, ST4 7QB, UK.

⁶ Department of Materials Science & Engineering, University of Florida, Gainesville, Florida USA

Abstract

Tumor hypoxia is associated with low rates of cell proliferation and poor drug delivery, limiting the efficacy of many conventional therapies such as chemotherapy. Since many macrophages accumulate in hypoxic regions of tumors, one way to target tumor cells in these regions could be to use genetically engineered macrophages that express therapeutic genes when exposed to hypoxia. We describe here our use of a new mathematical model to simulate and compare the effects of conventional cyclophosphamide therapy with those induced when macrophages are used to deliver hypoxia-inducible cytochrome P450 to locally activate cyclophosphamide. Our mathematical model describes the spatio-temporal dynamics of vascular tumor growth and treats cells as distinct entities, each with its own cell cycle and subcellular signalling machinery. Moreover, the model simulates the delivery of systemically-applied therapies by a dynamic vascular network. We used this model to determine both the impact on tumors of combining conventional chemotherapy with macrophage-based gene delivery, and how the efficacy of macrophage-based therapies may be enhanced by pre-loading the cells with magnetic nanoparticles and applying a magnetic field to the tumor site.

Major Findings—Our results predict that combining conventional and macrophage-based therapies would be synergistic, producing greater anti-tumor effects than the additive effects of each form of therapy. Moreover, we found that timing is crucial in this combined approach with efficacy being greatest when the macrophage-based therapy is administered shortly before or concurrent with chemotherapy. Lastly, we show not only that macrophage delivery of therapeutic

Requests for reprints: Markus Owen, School of Mathematical Sciences, University of Nottingham, Nottingham NG7 2RD, UK..

Disclosure of Potential Conflicts of Interest: J Dobson is a consultant to and shareholder in nanoTherics Limited, which is commercialising magnetic nanoparticle-based gene transfection technology. J Dobson, CE Lewis and HM Byrne are co-inventors of a relevant patent applied for by Keele University: Targeted Therapy. Patent Pending (Application Nos. 60/789,185; P112277GB; WO2007113572 – Filed: 2006).

genes is markedly enhanced using the magnetic approach described above, but also that the disorganised nature of tumor blood vessels means that this enhancement depends mainly on the strength of the applied field, rather than its direction. This may be important in the treatment of non-superficial tumors where generating a specific orientation of a magnetic field may prove difficult. In conclusion, we demonstrate that mathematical modelling can be used to design, and maximize the efficacy of, combined therapeutic approaches in cancer.

Keywords

macrophage; gene therapy; hypoxia; mathematical model; combination therapy

Introduction

Hypoxic areas of tumors are notoriously hard to target with conventional drugs (due to their poor vascularisation), yet treatment success often hinges upon the elimination of such areas since any remaining hypoxic tumor cells often secrete cytokines that cause the tumor to revascularise and regrow (1, 2). A possible anti-cancer strategy, outlined in Figure 1, exploits the innate ability of macrophages, a type of immune cell, to accumulate within hypoxic tumor regions (3, 4). Tumor spheroid experiments *in vitro* have shown that when macrophages are genetically modified to express a prodrug-activating enzyme (cytochrome P450) during hypoxia, tumor cell kill can be achieved (following conversion of the prodrug cyclophosphamide into its cytotoxic moiety by enzyme-expressing hypoxic macrophages) (3). For the same kind of treatment to be successful *in vivo*, assuming intravenous injection of the prodrug and macrophages, a substantial number of macrophages would need to extravasate from the bloodstream and localise at the tumor mass. To increase delivery to the tumor site, we have devised a magnetic approach in which monocytes (macrophage precursor cells, found in the bloodstream) are pre-loaded with magnetic nanoparticles by phagocytosis (5). *In vivo* experiments in mice have demonstrated the potential of this technique; systemic injection of such magnetic macrophages, in combination with application of an externally-applied magnetic field near the tumor, increased three-fold the number of macrophages accumulated within the tumor (5). However, such experiments have not yet been attempted using “therapeutically-armed” macrophages (i.e. macrophages that express a therapeutic gene). While these *in vitro* and *in vivo* experimental results are highly promising, a number of questions remain. For example, for the prodrug-enzyme pair used in the *in vitro* experiments (3), it is not clear which cells are targeted. Previous mathematical modelling of tumor spheroids suggests that whilst such engineered macrophages target active drug production to hypoxic regions, the dependence of tumor cell death on mitosis means that cell-kill is predominantly outside the hypoxic layer (6). It remains of interest to determine how the *in vitro* model predictions will translate to vascular tumors *in vivo*. It is also important to determine the *in vivo* efficacy of macrophage-based gene-therapy, to compare it to conventional therapies, to understand the possible synergistic benefits of combination therapy, and to assess the improvements in therapeutic outcomes that may be possible using the magnetic approach (5).

There is a long history of using mathematical models to study the growth of solid tumors and their response to therapy (7, 8, 9, 10). Compartmental models have been formulated as systems of ordinary differential equations (e.g. (11, 12)). Alternatively, partial differential equation (PDE) models have been proposed to explain the spatial structure within avascular tumor spheroids (6, 13) and the variations in vessel density within vascular tumors (14). Approaches that consider individual cells include models for angiogenesis and drug delivery (15), and hybrid models that also include PDE descriptions of tumor growth (16). A common feature of these models is that individual cells are represented as point objects, whereas alternative approaches represent cells as deformable spheres (17), or as a set of sites

on a lattice (18). In separate work, Alarcón and co-workers (19, 20, 21, 22) proposed a multiscale model for vascular tumor growth which combines blood flow, angiogenesis, vascular remodelling, and multiple interacting cell populations. This framework is unique in its extensive coupling across scales, exemplified by the way that vascular remodelling influences, and is influenced by, the growth dynamics of the cell populations, which are themselves regulated by models for subcellular signaling pathways including an oxygen-regulated cell cycle model (22).

Existing multiscale models of tumor growth differ in their emphasis on subcellular processes, cell-cell interactions, cell movement, nutrient delivery, and biomechanics. Most such models do not yet address issues of cancer therapy. There are several compartmental models for cancer therapy, addressing, for example, the emergence of a rapidly proliferating subpopulation under the selection pressure imposed by therapy (23); modelling immunotherapy (24); endothelial cell-targeted anti-Bcl-2 therapy (25), and modelling treatment via an oncolytic virus (26). Spatially-structured, PDE models for therapy include a study of anti-angiogenic gene therapy (27), and predictions of drug responses in breast cancer (28).

In this paper we extend the multiscale model of solid tumor growth (22) to account for conventional chemotherapy with cyclophosphamide, macrophage-based gene-therapy, and enhanced delivery of therapeutically-armed magnetic macrophages. Model simulations suggest that, compared to conventional chemotherapy, macrophage treatment may preferentially target tumor cells, and leave a smaller remaining fraction of hypoxic tumor cells. We also observe that, for tumors growing in tissues with relatively isotropic vascular networks (i.e. with no dominant vessel orientation), enhanced macrophage extravasation depends predominantly on the strength of the applied field, rather than its direction. Finally, we show how combination therapies may act in a strongly synergistic manner, particularly when macrophage-therapy is applied shortly before, or concurrent with, conventional therapy.

Quick Guide to Equations and Assumptions

We represent the tissue as a regular two-dimensional lattice (spacing Δx) with an embedded vascular network. Each site can contain a number of cells and has associated concentrations of oxygen, VEGF, prodrug and drug (Figure 1).

Major assumptions – Cells

Each normal and cancer cell has Ordinary Differential Equation models for the cell cycle and p53-VEGF signalling. On completion of the cell cycle, if space is available, daughter cells are placed at the same or a neighbouring site — otherwise the parent cell cycle restarts, and no daughter cell is produced. Cancer cells enter and leave quiescence according to the local oxygen concentration, and die if quiescent for too long. Normal cell apoptosis occurs if p53 exceeds a threshold which is lower when the cell is surrounded by cancer cells (so that the tumor microenvironment is hostile to normal cells).

All cell types move by a random walk, biased by the space available and gradients in VEGF. The probability of a cell moving from site \mathbf{x} to \mathbf{y} in time Δt is

Equation 1

$$\Pr(\mathbf{x}, \mathbf{y}, t) = \frac{D\Delta t}{2d_{\mathbf{x},\mathbf{y}}^2} \frac{(N_m - N(\mathbf{y}, t))}{N_m} \left(1 + \frac{\chi}{2D} (V(\mathbf{y}, t) - V(\mathbf{x}, t)) \right) \quad \text{for } \mathbf{x} \neq \mathbf{y}.$$

$N(\mathbf{x}, t)$ is the number of cells and $V(\mathbf{x}, t)$ the VEGF concentration at site \mathbf{x} . D is the maximum random motility, N_m the carrying capacity for movement, χ the chemotactic sensitivity ($\chi=0$ for normal and cancer cells), and $d_{\mathbf{x}, \mathbf{y}}$ the distance from \mathbf{x} to \mathbf{y} .

Major assumptions – Vasculature

We prescribe the pressure at a set of inlets and outlets, and compute the flow and pressure drop for each vessel segment (using the Poiseuille approximation) by imposing conservation of mass at each node. Vessel radii adapt to the wall shear stress, intravascular pressure, and flow (22, 29). We prescribe a haematocrit of 45% in vessels that sustain flow and zero otherwise. Segments with low flow are pruned if their wall shear stress remains below τ_w^{crit} for a period longer than T_{prune} .

Angiogenesis

On each time-step Δt , the probability of an endothelial tip cell sprouting from a vessel at site \mathbf{x} is

$$\text{Pr}_{\text{sprout}}(\mathbf{x}, t) = \Delta t \frac{P_{\text{sprout}}^{\max} V(\mathbf{x}, t)}{V_{\text{sprout}} + V(\mathbf{x}, t)}, \quad \text{Equation 2}$$

where V_{sprout} is the VEGF concentration at which the probability is half-maximal (22). $\text{Pr}_{\text{sprout}}(\mathbf{x}, t) = 0$ if the number of cells at \mathbf{x} exceeds the carrying capacity for sprouting, E_m^{tipcell} , or if a sprout has already emerged within an exclusion radius, R_{ex} (since Delta-Notch signalling inhibits adjacent cells from sprouting). Tip cells perform random walks, biased by VEGF, according to Eq. 1. When a tip cell moves, a stationary endothelial cell is left behind—thus sprout contiguity is maintained by endothelial cell proliferation (30). Anastomosis occurs when a tip cell moves to a site already occupied by a sprout or vessel, establishing flow in the new vessel. If anastomosis does not occur within T_{prune} of tip cell emergence, then the sprout dies.

Major assumptions – Diffusibles

Equations for oxygen, VEGF, drug and prodrug take the form:

$$0 = D_u \nabla^2 U + \rho_v \psi_u (U_{blood} - U) + S_u - \delta_u U, \quad \text{Equation 3}$$

where $U(\mathbf{x}, t)$ is the tissue concentration of interest, $U_{blood}(\mathbf{x}, t)$ the concentration in the blood, $S_u(\mathbf{x}, t)$ the cell- and environment-dependent production/removal rate, and δ_u the linear decay rate. $\rho_v(\mathbf{x}, t)$ is the vascular density and ψ_u the vascular permeability to U .

Major assumptions – Therapy

Conventional

Active drug is present in the blood plasma due to conversion of cyclophosphamide in the liver. After boluses at times T_n^q , plasma levels decay exponentially, so that the tissue drug concentration, $Q(\mathbf{x}, t)$, is governed by Eq. 3, with $S_q = 0$ and

$Q_{blood}(\mathbf{x}, t) = Q_{bolus} (1 - H(\mathbf{x}, t)) e^{-k_{qc}(t - T_n^q)}$ for $T_n^q \leq t < T_{n+1}^q$. Here, $H(\mathbf{x}, t)$ is the haematocrit in the vessel at \mathbf{x} .

Drug action

If $Q(\mathbf{x}, t) > Q_{crit}$ any cell at site \mathbf{x} intercalates active drug. Normal and cancer cells with drug intercalated die upon attempting cell-division.

Macrophages & magnetic field

On one time-step the probability of macrophage extravasation from a vessel at \mathbf{x} is

Equation 4

$$P_{\text{extra}}^{\text{mac}}(\mathbf{x}, t) = \Delta t 2\pi R(\mathbf{x}, t) L(\mathbf{x}, t) M_{\text{blood}}(\mathbf{x}, t) \frac{V(\mathbf{x}, t)}{A_v + V(\mathbf{x}, t)} \left(\alpha_m + \beta_m |\mathbf{v}_{\text{mag}} \cdot \mathbf{n}(\mathbf{x}, t)| \right)$$

where $R(\mathbf{x}, t)$ is the radius of the vessel (if present) through \mathbf{x} at time t , $L(\mathbf{x}, t)$ is the length of the vessel segment, $M_{\text{blood}}(\mathbf{x}, t) = k_M \frac{H(\mathbf{x}, t)}{H_{in}} e^{-k_{\text{mac}}(t - T_{\text{mac}})}$ is the macrophage level in the vessel following a single injection of macrophages (H_{in} is the reference inflow haematocrit), the extravasation rate increases with VEGF (31), and A_v is the VEGF concentration at which it is half-maximal. In Eq. 4, α_m represents the baseline extravasation rate and β_m determines the increase due to magnetic effects, \mathbf{v}_{mag} is the macrophage velocity due to the magnetic field, and the effect of the magnetic field is mediated by $|\mathbf{v}_{\text{mag}} \cdot \mathbf{n}(\mathbf{x}, t)|$, the component of \mathbf{v}_{mag} that points into the vessel wall (32). Extravasation can only occur if the number of cells at \mathbf{x} is less than E_m^{mac} . Tissue macrophages do not proliferate, have a normally distributed survival time (mean = 90 days, s.d. = 9 days), and move chemotactically according to Eq. 1 (33). This has no magnetic component since the magnetic force on macrophages in the tissue is negligible (see Supplementary Material).

The prodrug and active drug concentrations, $P(\mathbf{x}, t)$ and $Q(\mathbf{x}, t)$, are governed by Eq. 3, with $P_{\text{blood}}(\mathbf{x}, t) = P_{\text{bolus}} (1 - H(\mathbf{x}, t)) e^{-k_{\text{pc}}(t - T_n^p)}$ and $Q_{\text{blood}}(\mathbf{x}, t) = 0$. Active drug is produced from prodrug via hypoxic macrophages expressing cytochrome P450:

Equation 5

$$S_q(\mathbf{x}, t) = \begin{cases} k_{pq} P(\mathbf{x}, t) & \text{if a Macrophage is at } \mathbf{x} \text{ and } C(\mathbf{x}, t) < C_{\text{hyp}}, \\ 0 & \text{otherwise.} \end{cases}$$

Prodrug conversion means that $S_p(\mathbf{x}, t) = -S_q(\mathbf{x}, t)$.

Materials and Methods

The main components of the multiscale model are described in detail in (22). New features introduced in this paper include tissue macrophages (and the effect of magnetic nanoparticles on their extravasation), additional diffusible species (drug and prodrug), the effect that the active drug moiety has on proliferating cells, and the local conversion of prodrug to drug by hypoxic macrophages. Figure 1 illustrates the model framework, and the **Quick Guide to Equations and Assumptions** provides an overview of the key model components. Further model details and parameter values can be found in the supplementary material and in (22).

The model is formulated on a regular two-dimensional lattice with an embedded vascular network. Each lattice site can contain a number of cells of different types and has associated concentrations of oxygen, Vascular Endothelial Growth Factor (VEGF), prodrug and drug. Different submodels describe behaviour at the subcellular, cellular and macroscopic (diffusible and vascular) scales. The spatial scales of interest range from 10 μm (cells, vessel diameters) to mm (tissue size), while the timescales vary from minutes (signalling, protein synthesis), to hours (cell proliferation and movement) and days/weeks (tumor doubling time, angiogenesis). Coupling between the different submodels is achieved in several ways. For

example, local oxygen levels, which are determined at the macroscale, influence both cell cycle progression and VEGF production at the subcellular level. Conversely, VEGF production modulates angiogenesis at the macroscale and this, in turn, controls oxygen delivery to the tissue. In particular, lack of oxygen stimulates VEGF expression, which promotes macrophage extravasation and angiogenesis. In the vascular layer, the vessel radii are updated using a structural adaptation law similar to that proposed by Pries et al. (22, 29). We stress that the submodels we use illustrate how such a multiscale model can be assembled: the framework we present is general, with considerable scope for incorporating alternative submodels.

A particular form of conventional chemotherapy is modelled by assuming that the prodrug cyclophosphamide (CPA) is delivered systemically and is converted by the enzyme cytochrome P450, principally in the liver, to its active, cytotoxic moiety. Hence, for conventional chemotherapy we model the pharmacokinetics of the active moiety blood concentration by exponential decay following weekly boluses of CPA. For macrophage-based gene therapy, we model macrophage extravasation and chemotactic migration to hypoxic regions, in order to deliver hypoxia-inducible-cytochrome P450 to hypoxic areas of tumors, hence localising CPA conversion to those regions. To model the enhanced delivery of macrophages loaded with magnetic nanoparticles, we modify the extravasation rate accordingly (see Eq. 4 and the supplementary material). As magnetic nanoparticle-loaded macrophages approach the high-field region, the z-axis component of the field gradient dominates so that the particles are generally pulled towards the magnetic field source. Once macrophages have extravasated, we do not include any magnetic component to their movement, since the magnetic force on macrophages in the tissue is negligible (see supplementary material).

For each control and therapeutic scenario considered we performed multiple virtual tissue simulations (stochastic realisations). Since cell movements, angiogenic sprouting and macrophage extravasation are probabilistic processes, on each time step different simulations (generated by different initialisations of a random number generator) can yield subtly different outcomes, which can lead to significant changes in long-term behaviour. Thus it is essential to consider both the mean behaviour and the degree of variation between simulations.

We used our model to generate ten simulations of a normal tissue, in a $2\text{mm} \times 2\text{mm}$ domain, with a reproducible characteristic vascular density (vascular surface area per unit volume, $\text{mean} \pm \text{standard error} = 9.9 \pm 0.19 \text{ mm}^2/\text{mm}^3$). Implanting a small tumor into such a computational tissue leads to the spread of the tumor, which develops regions of hypoxia and stimulates angiogenesis, such that after 100 days the tissue has a higher vascular density ($18.6 \pm 0.23 \text{ mm}^2/\text{mm}^3$), and a quiescent fraction of $8.2 \pm 0.74\%$ (percent of cancer cells that are quiescent). These values are consistent with published data (see Section D.1 of the supplementary material for further details of model validation). We then applied therapy to these simulated tumors, using conventional chemotherapy, macrophage-based gene therapy (with and without enhancement using magnetic nanoparticles), and various combinations.

Results

Conventional chemotherapy

Figure 2A shows snapshots from a typical simulation in which conventional chemotherapy is applied in weekly boluses beginning three weeks after tumor implantation. After each bolus, the active drug concentration is maximal close to blood vessels, but otherwise relatively homogeneously distributed throughout the tissue. A significant number of cells are killed following each treatment, in locations where cell proliferation coincides with a high

drug concentration. Cancer cells are preferentially targeted because their rates of proliferation are higher than those for normal cells, but the tumor recovers after each treatment. Figure 2B shows the average rate of cell division, drug concentration and rate of cell kill from day 21 (the start of therapy) to day 100, and reinforces the perception that the drug distribution and cell-kill are widespread and indiscriminate.

Figure 4A shows how the total numbers of normal and cancer cells change over time, in the simulated tissue, for control (no therapy) and conventional therapy. For the ten therapeutic simulations, the tumor cell number declines dramatically following each drug bolus, and then recovers before the next treatment. The drug dose is insufficient to eliminate all tumor cells, and hence the tumor eventually colonises the entire domain after the final round of therapy. For these examples (of control and unsuccessful conventional therapy) the number of normal cells drops to zero, and the total tumor cell number is limited. These outcomes are artefacts of the limited size of the *in silico* tissue domain: *in vivo* the tumor would be embedded in a larger tissue and surrounded by more normal cells.

Figure 5A illustrates dose-response data (at 100 days after tumor implantation, i.e. 2 days after the 12th treatment) as the maximal concentration of active drug in the blood (Q_{bolus}) varies. As the dose increases, the tumor burden decreases, with a half maximal effective concentration (EC₅₀) of $Q_{bolus} \approx 12$. For smaller doses, the quiescent fraction increases relative to control. For sufficiently large doses the tumor is eliminated, although too large a dose prevents normal tissue recovery.

Macrophage therapy

Figure 3A shows snapshots from a typical simulation of macrophage therapy (see Supplementary Movie 1). Three weeks after tumor implantation a single bolus of macrophages is applied, together with the first of 20 weekly doses of prodrug. The individual snapshots and cumulative data (Figure 3B) show that the macrophage therapy targets hypoxic cells but does not kill them when they are hypoxic (macrophages and drug are co-located, but cell-kill occurs in a band outside this area). In spite of this, cell-kill is predominantly in a region that is complementary to that for conventional therapy, and macrophage therapy preferentially targets tumor cells rather than normal cells.

Figure 4B shows the temporal dynamics of cell numbers in the simulated tissue. We show the mean in the control case, and the mean and ten simulations for macrophage therapy. Each therapeutic simulation follows a similar temporal pattern. In some cases the tumor is almost eliminated at $t \approx 23$ days. At intermediate times (60-90 days) the impact of successive treatments diminishes, since the tumor does not develop the degree of hypoxia seen for the first round of treatment, and hence prodrug activation is less extensive. At about 90 days the macrophages begin to die, and the therapeutic effect declines until after day 130 it is negligible.

For this prodrug dose ($P_{bolus}=250$) the reduction in overall tumor burden (compared to untreated control) is similar to that for conventional therapy with $Q_{bolus}=12$ (compare the tumor cell numbers in Figure 4A and B), and both cases correspond approximately to half-maximal efficacy (see Figure 5). However, the quiescent fraction at 100 days is lower with this example of macrophage therapy ($6 \pm 0.48\%$) than with the equivalent conventional therapy ($11.3 \pm 1.7\%$), indicating that the macrophage therapy preferentially targets hypoxic tumor cells. In addition, at early times (21-50 days) the normal cell population declines more slowly with macrophage therapy than in either the control or conventionally treated cases. Figure 5B illustrates dose-response data for macrophage therapy, showing half-maximal efficacy at $P_{bolus} \approx 250$. For $P_{bolus} > 50$, the quiescent fraction decreases with prodrug dose.

For sufficiently large doses the tumor is eliminated, although too large a dose is harmful to normal tissue.

Effect of magnetic nanoparticles on macrophage extravasation

Experiments *in vivo* have shown a threefold enhancement in the infiltration of macrophages loaded with magnetic nanoparticles (macrophage proportion of tumor mass: 4.9% without, and 16.9% with, a magnetic field) (5). We determined parameter values so that simulated infiltration into ten established tumors, with differing emergent vascular networks, gave the same degree of magnetic enhancement. Figure 6A shows that, at 5 hours, the mean proportion of macrophages (over ten simulations) is $4.9 \pm 0.6\%$ in the absence of the magnetic field. This increases to $15.8 \pm 1.3\%$ ($17.9 \pm 1.5\%$) with the field in the horizontal (vertical) direction. Over one week we see a pattern of rapid infiltration followed by a gradual settling to a steady density in the tissue, as the level of macrophages in the bloodstream falls to zero. This infiltration has a weak effect on the size of the tumor (Figure 6A). Figure 6B shows the cumulative locations of macrophage extravasation after 5 hours, illustrating that the magnetic field increases the extravasation rate at specific vessels according to their orientation relative to the magnetic field. Nevertheless, Figure 6C shows that the overall pattern of macrophage localisation within the tissue is similar for both orientations of the field.

Combination therapies

Figure 4C summarises results from simulations combining the conventional and macrophage therapies illustrated in Figures 2 and 3. Three weeks after tumor implantation a single bolus of macrophages is applied, together with the first of 20 weekly doses of prodrug and active drug. In all ten simulations, the combined treatment eliminates the tumor, and in 8/10 cases the normal tissue recovers. This might be expected, since the individual conventional and macrophage therapies gave 54% and 45% reductions in tumor size respectively. Therefore, we consider whether there are synergistic benefits of combination therapies where the individual therapies have smaller efficacies.

Figure 7A summarises the results for the control case and seven therapeutic combinations (conventional alone, $Q_{bolus}=11$; macrophages alone, $P_{bolus}=120$; and combinations with and without magnetic enhancement). The conventional and macrophage therapies have a limited effect on the tumor size (average reductions of 27% and 21% respectively), but combining them gives an average reduction of 94%. However, the outcome is highly variable (for time courses see Figure S5 of the supplementary material). In 6/10 cases the tumor is eliminated (supplementary Movie 2 shows an example of tumor elimination); in the remaining four cases the tumor is reduced in size during treatment, but regrows after the last round of therapy. Combining macrophages with magnetic nanoparticles and a magnetic field gives a significant improvement over macrophages alone, due to the increased macrophage infiltration and consequently higher levels of prodrug activation within the tumor. The results with $Q_{bolus}=11$, $P_{bolus}=120$ (tumor elimination in 6/10 cases) can be improved further by combining conventional drug delivery with macrophages *and* enhancing macrophage extravasation using magnetic nanoparticles; the tumor is eliminated in 10/10 simulations, for both directions of the magnetic field (Figure 7A).

Finally, delivering macrophage after conventional therapy gives worse outcomes over a range of lags from 1 hour up to 4 days (Figure 7B). Macrophage therapy 1 hour *before* conventional therapy is beneficial, with tumor elimination in 7/10 cases (rather than 6/10 with simultaneous delivery). However, greater timing differences again give worse outcomes. Additional examples of combination therapy and altered timing can be found in Figure S6 of the Supplementary Material.

Discussion

We have extended a multiscale mathematical model of vascular tumor growth to simulate the response to conventional chemotherapy and a new, macrophage-based gene therapy that targets hypoxic tumor regions. We also use the model to investigate the potential for enhancing the delivery of such macrophage-based therapies by pre-loading macrophages with magnetic nanoparticles and applying a magnetic field near the tumor. The overarching aim of this work is to build upon data from *in vitro* and *in vivo* experiments (3, 5) in order to generate experimentally testable predictions and hypotheses about a novel therapeutic strategy.

Our model simulations indicate that the macrophage-based therapy, with hypoxia-inducible cytochrome P450 activating cyclophosphamide, targets hypoxic cells but does not kill them when they are hypoxic. The macrophage-based therapy is more effective against tumor cells than normal ones, because of the greater degree of hypoxia found in tumor compared to normal tissue. While both conventional and macrophage-based approaches may yield similar reductions in tumor volume, the hypoxic volume fraction of the macrophage-treated tumor is typically smaller than that of its conventionally-treated counterpart, making the tumor more responsive to follow-on treatment with drugs that target rapidly proliferating cells. Consequently, it is unsurprising that combination therapy is synergistic, yielding reductions in tumor volume in excess of those expected if the treatments act independently. When macrophage treatment is successful, it is self-limiting in nature, since elimination of the tumor also eliminates the hypoxia that drives the therapeutic effect. Magnetically loading the macrophages enhances their effect, and, for the relatively isotropic vascular networks studied here, the increase in delivery does not depend strongly on the direction of the magnetic field. Since tumor blood vessels are often highly disorganized (34), this result may be important for non-superficial tumors, for which it may be difficult to generate a magnetic field with a specific orientation. In many cases, we find considerable variability in outcomes — the same treatment applied to different simulated tissues may either successfully eliminate the tumor or allow it to persist. Hence it is essential to consider, as in this paper, multiple virtual tissue simulations in order to capture average behaviour and the degree of variation that can be expected. Finally, we find that, for combination therapies, timing can be crucial — it is best to apply macrophage therapy slightly in advance of conventional therapy.

We have investigated the sensitivity of the anti-tumor response to variations in key therapeutic parameters. Our simulations reveal that the response to conventional and macrophage-based therapies is nonlinear: close to the EC_{50} , small changes in drug/prodrug dose produce large changes in the anti-tumor response, but away from the EC_{50} the dose-response relationship is relatively flat (Figure 5). Our major findings about the predicted synergy and timing dependence of combination therapy persist for different drug and prodrug doses (compare Figure 7 and Figure S6 of the supplementary text). Our results are also robust to changes in cell cycle times, and in the order in which the components of the computational algorithm are executed (see Section D and Figures S7 and S8 of the supplementary text).

A major advantage of simulations such as those used here is that it is possible to interrogate closely the state of the system as it develops over time, in order to identify key features that regulate the therapeutic response. Here we have used this approach to go beyond macroscopic measures (such as tumor size and hypoxic fraction) and to characterise where within the tissue the therapy is active, and how this relates to, for example, regions of hypoxia, macrophage localisation and cell proliferation. In future work it would be interesting to track the positions of cells when they intercalate drug (i.e. when they became

committed to drug-induced cell death), to assess the extent to which cells move out of hypoxic regions and then die, and to compare this with the extent to which they intercalate drug outside of the hypoxic region. We anticipate that this balance will depend on the degree of tumor cell motility.

Our results suggest many directions for future experimental research in this area. For example, the simulations reveal that the enzyme-prodrug combination considered here produces high levels of active drug in hypoxic regions, but kills cells in surrounding, non-hypoxic zones (similar results were obtained from a PDE model for macrophage gene therapy (6)). This feature arises because cell-kill requires attempted cell-division, which occurs preferentially at higher oxygen concentrations. It should be feasible experimentally to test our predictions about the locations of drug production and therapeutic tumor cell lysis by, for example, immunohistochemical staining of tissue sections to locate active drug, sites of DNA replication, and apoptotic cells. Supplementary staining for hypoxia and endothelial cells would provide additional spatial information against which to test our model predictions.

A number of model extensions are possible to investigate alternative therapies and to improve the applicability of our model. For example, we could investigate the efficacy of macrophages engineered to deliver anti-angiogenic or other vascular-targeting agents. Alternatively, we could simulate the effect of combining cytotoxic macrophage-based therapy (e.g. using cyclophosphamide) with vascular-disrupting agents such as Combretastatin A-4 (35), which we would expect to increase tumor hypoxia (and hence enhance prodrug activation). Our model could also be used to investigate whether application of an alternating field to the tissue containing the magnetically-loaded macrophages can generate a sufficiently large (and localised) heating effect to stimulate cell death in that region (36). On the other hand, it may be important to consider the potential pro-tumor effects of macrophages (such as the secretion of angiogenic factors) (37), and how a patient's blood monocytes and resident tissue macrophages might compete with the introduced genetically modified macrophages. Other related therapies that our model could be adapted to study include gene transfer of cytochrome p450 into tumor cells (38), and the use of macrophages to target a therapeutic virus to hypoxic tumor regions, under the control of a tumor tissue specific promoter (39). The latter avoids potential problems of prodrug activation at non-tumor sites of hypoxia, such as may be found in patients with atherosclerotic plaques or rheumatoid arthritis (40). In the future we will extend our model to 3 space dimensions. Based on results comparing untreated tumor growth in 2D and 3D¹, we anticipate that the qualitative behaviour will be unchanged for the various individual and combined therapies studied here.

In conclusion, we have demonstrated how our state-of-the-art mathematical model of vascular tumor growth can be used to test the efficacy of a new anti-cancer treatment and to support a programme of experimental work to optimise its efficacy. Our model provides insight into the *in vivo* mechanism of action of macrophage-based therapy, and can be used to generate experimentally-testable predictions (for example, that using macrophage therapy in combination with standard chemotherapy will provide synergistic benefits, and that such therapies should be administered near-simultaneously to achieve the best response). Our modelling can help to identify the most productive avenues for using macrophages as a novel system to deliver gene therapy, and can be extended to consider a variety of alternative therapeutic strategies.

¹H Perfahl, H M Byrne, T Chen, V Estrella, T Alarcón, A Lapin, R A Gatenby, R J Gillies, MC Lloyd, P K Maini, M Reuss, M R Owen: Multiscale modelling of vascular tumor growth in 3D: the roles of domain size and boundary conditions, submitted.

Supplementary Material

Refer to Web version on PubMed Central for supplementary material.

Acknowledgments

Financial support: Biotechnology and Biological Sciences Research Council, UK, BB/C506113/1, E18414 (Lewis), BB/C506156/1 (Richardson, Byrne, Stamper), BB/C506172/1 (Dobson), and E18413 (Owen, Byrne). Engineering and Physical Science Research Council, UK, EP/D501083/1 (Owen).

References

1. Vaupel P, Mayer A. Hypoxia in cancer: significance and impact on clinical outcome. *Cancer Metastasis Rev.* 2007; 26:225–239. [PubMed: 17440684]
2. Vaupel P. Hypoxia and Aggressive Tumor Phenotype: Implications for Therapy and Prognosis. *The Oncologist.* 2008; 13:21–26. [PubMed: 18458121]
3. Griffiths L, Binley K, Iqbal S, Kan O, Maxwell P, Ratcliffe P, Lewis C, Harris A, Kingsman S, Naylor S. The macrophage - a novel system to deliver gene therapy to pathological hypoxia. *Gene Therapy.* 2000; 7:255–262. [PubMed: 10694803]
4. Murdoch C, Lewis CE. Macrophage migration and gene expression in response to tumor hypoxia. *Int. J. Cancer.* 2005; 117:701–708. [PubMed: 16106399]
5. Muthana M, Scott SD, Farrow N, Morrow F, Murdoch C, Grubb S, Brown N, Dobson J, Lewis CE. A novel magnetic approach to enhance the efficacy of cell-based gene therapies. *Gene Therapy.* 2008; 15:902–910. [PubMed: 18418420]
6. Webb SD, Owen MR, Byrne HM, Murdoch C, Lewis CE. Macrophage-Based Anti-Cancer Therapy: Modelling Different Modes of Tumour Targeting. *Bull. Math. Biol.* 2007; 69:1747–1776. [PubMed: 17333419]
7. Araujo RP, McElwain DL. A history of the study of solid tumour growth: the contribution of mathematical modelling. *Bull. Math. Biol.* 2004; 66:1039–1091. [PubMed: 15294418]
8. Byrne HM. Dissecting cancer through mathematics: from the cell to the animal model. *Nat. Rev. Cancer.* 2010; 10:221–230. [PubMed: 20179714]
9. Lowengrub JS, Frieboes HB, Jin F, Chuang Y-L, Li X, Macklin P, Wise SM, Cristini V. Nonlinear modelling of cancer: bridging the gap between cells and tumours. *Nonlinearity.* 2010; 23:R1. [PubMed: 20808719]
10. Tracqui P. Biophysical models of tumour growth. *Rep. Prog. Phys.* 2009; 72:056701.
11. Arakelyan L, Vainstein V, Agur Z. A computer algorithm describing the process of vessel formation and maturation, and its use for predicting the effects of anti-angiogenic and anti-maturation therapy on vascular tumor growth. *Angiogenesis.* 2002; 5:203–14. [PubMed: 12831061]
12. Arakelyan L, Merbl Y, Agur Z. Vessel maturation effects on tumour growth: validation of a computer model in implanted human ovarian carcinoma spheroids. *Eur. J. Cancer.* 2005; 41:159–167. [PubMed: 15618001]
13. Greenspan HP. On the growth and stability of cell cultures and solid tumors. *J. Theor. Biol.* 1976; 56:229–242. [PubMed: 1263527]
14. Breward CJW, Byrne HM, Lewis CE. A multiphase model describing vascular tumour growth. *Bull. Math. Biol.* 2003; 65:609–640. [PubMed: 12875336]
15. McDougall SR, Anderson ARA, Chaplain MAJ. Mathematical modelling of dynamic adaptive tumour-induced angiogenesis: Clinical implications and therapeutic targeting strategies. *J. Theor. Biol.* 2006; 241:564–89. [PubMed: 16487543]
16. Macklin P, McDougall S, Anderson AR, Chaplain MAJ, Cristini V, Lowengrub J. Multiscale modelling and nonlinear simulation of vascular tumour growth. *J. Math. Biol.* 2009; 58:765–798. [PubMed: 18781303]
17. Drasdo, D.; Jagiella, N.; Ramis-Conde, I.; Vignon-Clementel, I.; Weens, W. Modeling steps from a benign tumor to an invasive cancer: examples of intrinsically multi-scale problems. In: Chauviere,

- A.; Preziosi, L.; Verdier, C., editors. *Cell Mechanics: From Single Scale-Based Models to Multiscale Modeling*. Chapman & Hall/CRC; 2010. p. 379-417.
18. Shirinifard A, Gens JS, Zaitlen BL, Poplawski NJ, Swat M, Glazier JA. 3D Multi-Cell Simulation of Tumor Growth and Angiogenesis. *PLoS One*. 2009; 4:e7190. [PubMed: 19834621]
 19. Alarcon T, Byrne HM, Maini PK. A cellular automaton model for tumour growth in inhomogeneous environment. *J. Theor. Biol.* 2003; 225:257–274. [PubMed: 14575659]
 20. Alarcon T, Byrne HM, Maini PK. A Multiple Scale Model for Tumor Growth. *Multiscale Model. Sim.* 2005; 3:440–475.
 21. Alarcon T, Owen MR, Byrne HM, Maini PK. Multiscale modelling of tumour growth and therapy: the influence of vessel normalisation on chemotherapy. *Comput. Math. Methods Med.* 2006; 7:85–119.
 22. Owen MR, Alarcón T, Maini PK, Byrne HM. Angiogenesis and vascular remodelling in normal and cancerous tissues. *J. Math. Biol.* 2009; 58:689–721. [PubMed: 18941752]
 23. Castorina P, Carcò D, Guiot C, Deisboeck TS. Tumor growth instability and its implications for chemotherapy. *Cancer Res.* 2009; 69:8507–8515. [PubMed: 19861540]
 24. Cappuccio A, Elishmereni M, Agur Z. Cancer immunotherapy by interleukin-21: potential treatment strategies evaluated in a mathematical model. *Cancer Res.* 2006; 66:7293–7300. [PubMed: 16849579]
 25. Jain HV, Nör JE, Jackson TL. Quantification of endothelial cell-targeted anti-Bcl-2 therapy and its suppression of tumor growth and vascularization. *Mol. Cancer Ther.* 2009; 8:2926–2936. [PubMed: 19808978]
 26. Wein LM, Wu JT, Kirn DH. Validation and analysis of a mathematical model of a replication-competent oncolytic virus for cancer treatment: implications for virus design and delivery. *Cancer Res.* 2003; 63:1317–1324. [PubMed: 12649193]
 27. Billy F, Ribba B, Saut O, Morre-Trouillet H, Colin T, Bresch D, Boissel JP, Grenier E, Flandrois JP. A pharmacologically based multiscale mathematical model of angiogenesis and its use in investigating the efficacy of a new cancer treatment strategy. *J. Theor. Biol.* 2009; 260:545–562. [PubMed: 19615383]
 28. Frieboes HB, Edgerton ME, Fruehauf JP, Rose FR, Worrall LK, Gatenby RA, Ferrari M, Cristini V. Prediction of drug response in breast cancer using integrative experimental/computational modeling. *Cancer Res.* 2009; 69:4484–4492. [PubMed: 19366802]
 29. Pries AR, Reglin B, Secomb TW. Structural adaptation of microvascular networks: functional roles of adaptive responses. *Am. J. Physiol. Heart Circ. Physiol.* 2001; 281:H1015–25. [PubMed: 11514266]
 30. Jackson T, Zheng X. A Cell-based Model of Endothelial Cell Migration, Proliferation and Maturation During Corneal Angiogenesis. *Bull. Math. Biol.* May 01.2010 72:830–868. [PubMed: 20052558]
 31. Claus M, Gerlach M, Gerlach H, Brett J, Wang F, Familletti PC, Pan YC, Olander JV, Connolly DT, Stern D. Vascular permeability factor: a tumor-derived polypeptide that induces endothelial cell and monocyte procoagulant activity, and promotes monocyte migration. *J. Exp. Med.* 1990; 172:1535–1545. [PubMed: 2258694]
 32. Grief AD, Richardson G. Mathematical modelling of magnetically targeted drug delivery. *J. Magn. Mater.* 2005; 293:455–463.
 33. Barleon B, Sozzani S, Zhou D, Weich H, Mantovani A, Marme D. Migration of human monocytes in response to vascular endothelial growth factor (VEGF) is mediated via the VEGF receptor flt-1. *Blood.* 1996; 87:3336–3343. [PubMed: 8605350]
 34. Munn LL. Aberrant vascular architecture in tumors and its importance in drug-based therapies. *Drug Discov. Today.* 2003; 8:396–403. [PubMed: 12706657]
 35. Tozer GM, Kanthou C, Baguley BC. Disrupting tumour blood vessels. *Nat. Rev. Cancer.* 2005; 5:423–435. [PubMed: 15928673]
 36. Ito A, Tanaka K, Kondo K, Shinkai M, Honda H, Matsumoto K, Saida T, Kobayashi T. Tumor regression by combined immunotherapy and hyperthermia using magnetic nanoparticles in an experimental subcutaneous murine melanoma. *Cancer Sci.* 2003; 94:308–313. [PubMed: 12824927]

37. Coffelt SB, Hughes R, Lewis CE. Tumor-associated macrophages: Effectors of angiogenesis and tumor progression. *BBA - Rev. Cancer*. 2009; 1796:11–18.
38. Gunther M, Waxman D, Wagner E, Ogris M. Effects of hypoxia and limited diffusion in tumor cell microenvironment on bystander effect of P450 prodrug therapy. *Cancer Gene Ther*. 2006; 13:771–779. [PubMed: 16543915]
39. Muthana M, Giannoudis A, Scott S, Fang H-Y, Coffelt S, Morrow F, Murdoch M, Burton J, Cross N, Burke B, Mistry R, Hamdy F, Brown N, Georgopoulos L, Hoskin P, Essand M, Lewis C, Maitland N. Use of Macrophages to Target Therapeutic Adenovirus to Human Prostate Tumors. *Cancer Res*. 2011 OnlineFirst.
40. Murdoch C, Muthana M, Lewis CE. Hypoxia Regulates Macrophage Functions in Inflammation. *J. Immunol*. 2005; 175:6257–6263. [PubMed: 16272275]

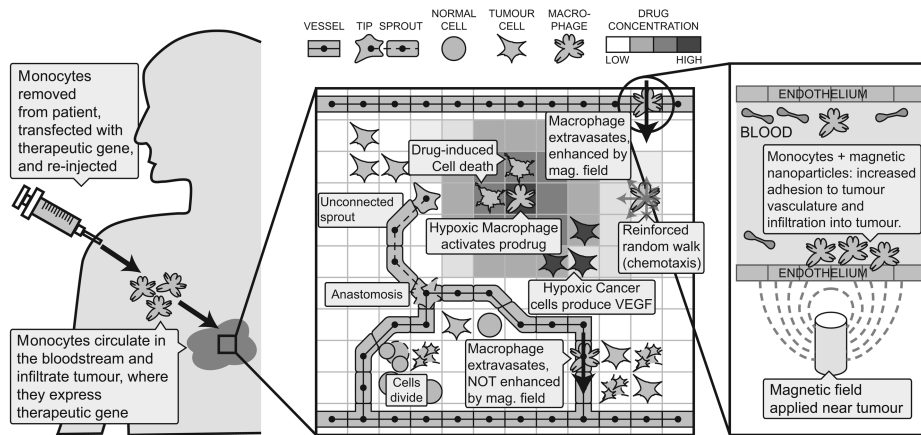


Figure 1. Outline of macrophage-based cancer therapy and mathematical model framework. Key interactions are shown, in particular that tissue oxygen depends on the vascular layer, that VEGF drives angiogenesis and macrophage migration, that drug kills tumor cells, and that hypoxic macrophages activate prodrug under hypoxia. In addition, extravasation of macrophages loaded with magnetic nanoparticles is enhanced most strongly in vessels that are perpendicular to the direction of action of a magnetic field.

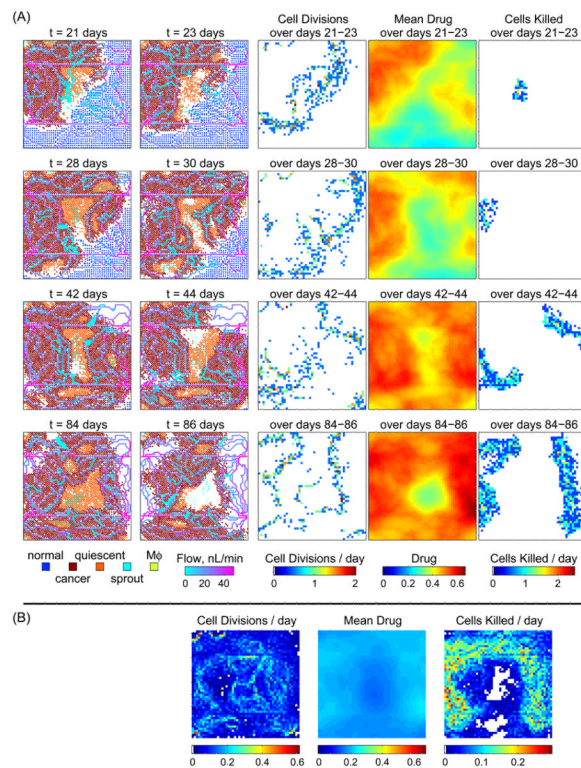


Figure 2.

Typical simulation showing how a tumor responds to conventional chemotherapy with cyclophosphamide, via weekly boluses ($Q_{bolus}=12$) that start three weeks after tumor implantation. **(A)** The state of the simulated tissue before and two days after treatments at $t=21$, 28, 42 and 84 days, and the average rate of cell division, drug concentration and rate of cell-kill over each 2-day period. **(B)** The rate of cell division, average drug concentration and rate of cell-kill over days 21 to 100.

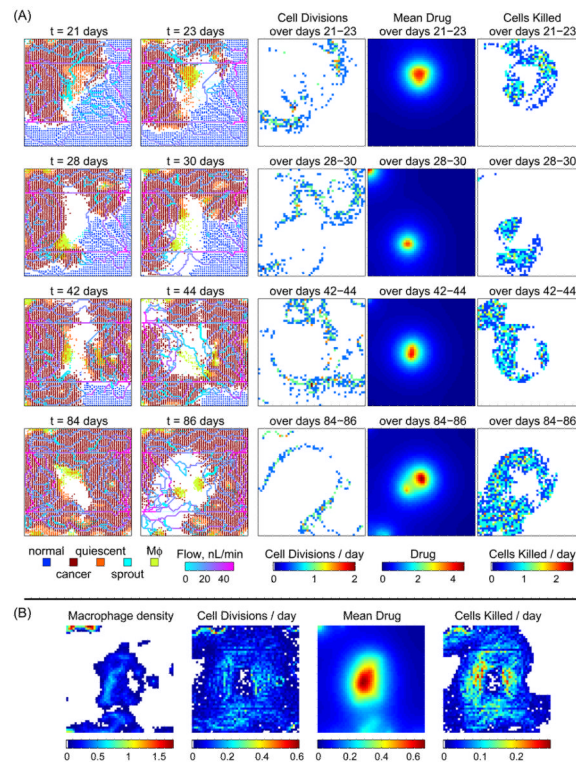


Figure 3.

Typical simulation of macrophage therapy via a single bolus of engineered macrophages three weeks after tumor implantation, coincident with the first of 20 weekly boluses of the prodrug cyclophosphamide ($P_{bolus}=250$). **(A)** The state of the simulated tissue before and two days after treatments at $t=21$, 28, 35 and 84 days, and the average rate of cell division, drug concentration and rate of cell-kill over each 2-day period. **(B)** The average macrophage density, rate of cell division, drug concentration, and rate of cell-kill over days 12 to 100.

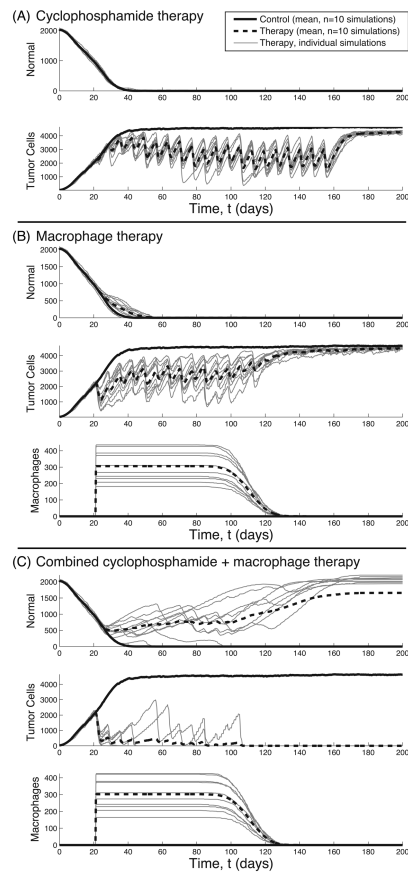


Figure 4.

The response to therapy over time. **(A)** Conventional therapy, $Q_{bolus}=12$. Each bolus leads initially to tumor regression and then regrowth. **(B)** Engineered macrophages accumulate after injection on day 21. Weekly prodrug boluses ($P_{bolus}=250$) cause the tumor to shrink initially and then to regrow. **(C)** Engineered macrophages *and* conventional therapy ($P_{bolus}=250$, $Q_{bolus}=12$). In 10/10 simulations the tumor is eliminated and normal tissue recovers in 8/10 cases. (Colour version: Fig. S4 in supplement)

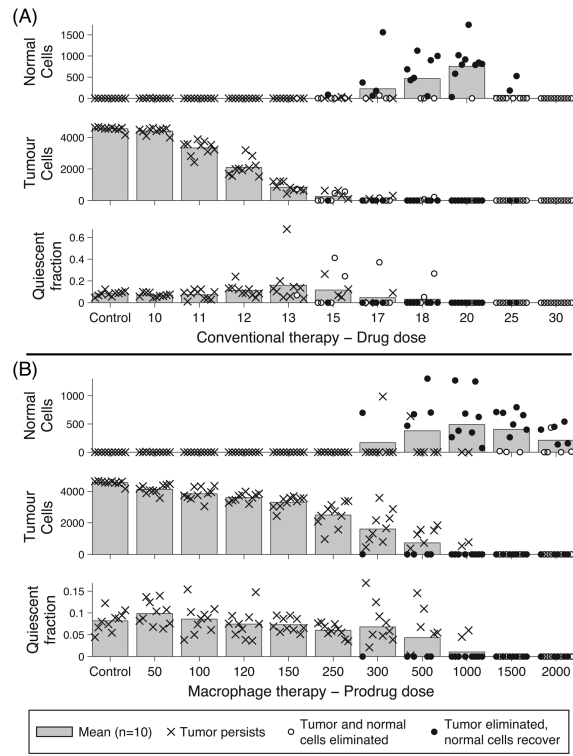


Figure 5.

Dose-response data at 100 days for tumor growth with conventional and macrophage therapy. **(A)** Response to conventional therapy across a range of drug doses (Q_{bolus}). Half-maximal efficacy is reached at $Q_{bolus} \approx 12$. **(B)** Response to macrophage therapy across a range of prodrug doses (P_{bolus}). Half-maximal efficacy is reached at $P_{bolus} \approx 250$. **(A,B)** In both cases, drug/prodrug doses above the EC_{50} can promote recovery of normal tissue, but if the dose is too large normal tissue is also damaged further. Bars represent mean values ($n=10$) and individual simulations are indicated by points. The point style indicates whether or not the tumor and/or normal cells persist at the end of each simulation (at 200 days).

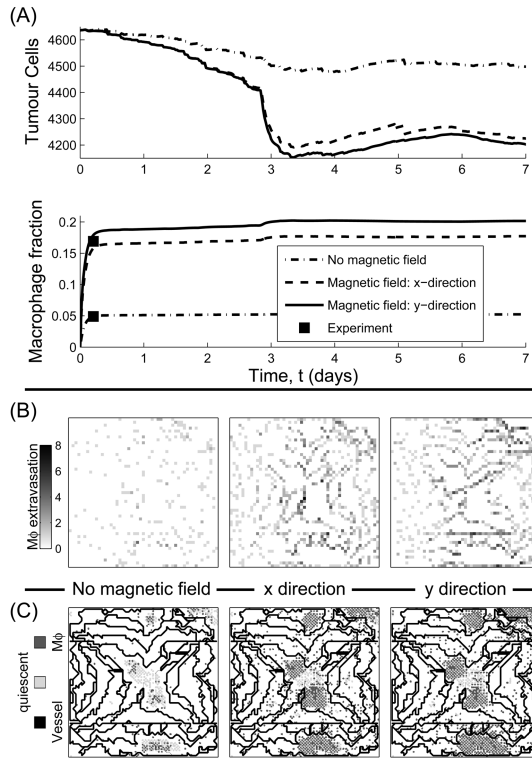


Figure 6.

(A) Series of curves showing dependence on the magnetic field of macrophage infiltration into a tumor, where the macrophages have been loaded with magnetic nanoparticles. Each curve is the mean of ten simulations. The macrophage fractions after five hours, without and with a magnetic field, are in agreement with experimental data in (5). (B) Cumulative macrophage extravasation at five hours, without a magnetic field, and with a magnetic field oriented in the x - and y -directions. The magnetic field increases the extravasation rate at specific vessels according to their orientation relative to the magnetic field. (C) The distribution of quiescent cancer cells, infiltrated macrophages, and the vascular network at five hours. The overall pattern of macrophage localisation is similar for both orientations of the field.

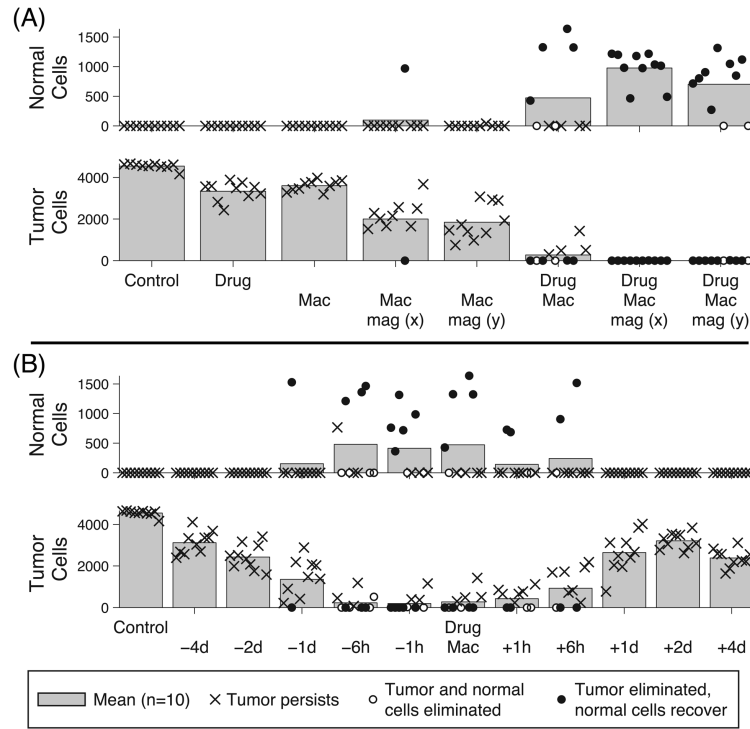


Figure 7. Summary data, showing the state at 100 days, for combination therapies starting three weeks after tumor implantation. **(A)** Comparison of conventional therapy ($Q_{bolus}=11$), macrophage therapy ($P_{bolus}=120$), magnetically enhanced macrophage therapy, and simultaneously delivered combinations. For combined conventional and macrophage therapy, the average reduction in tumor size is greater than would be expected from the sum of the individual effects. The results also illustrate the variability in response that can occur. **(B)** One combination ($Q_{bolus}=120$, $Q_{bolus}=11$), which gives tumor elimination in 6/10 cases, with various timing shifts of macrophage therapy relative to conventional therapy. “-1h” indicates macrophage therapy is 1 hour before conventional therapy, etc. Macrophage therapy 1h and 6h prior to conventional therapy gives a small advantage (tumor elimination in 7/10 cases). All other tested timing shifts give worse responses. **(A,B)** Bars represent mean values (n=10) and individual simulations are indicated by points. The point style indicates whether or not the tumor and/or normal cells persist at the end of each simulation (at 200 days).